

# Soil Attenuation in Seismic Simulations: Implications for Vehicle Tracking

September 2001

Stephen A. Ketcham<sup>1</sup>, Roy J. Greenfield<sup>2</sup>, Mark L. Moran<sup>1</sup>, Thomas S. Anderson<sup>1</sup>, and Stig O. Hestholm<sup>3</sup>

<sup>1</sup>USACE Engineer Research and Development Center, Cold Regions Research and Engineering Laboratory (ERDC-CRREL), 72 Lyme Rd, Hanover, NH 03755,  
Stephen.A.Ketcham@erdc.usace.army.mil

<sup>2</sup>Penn State University

<sup>3</sup>University of Texas at Dallas

## ABSTRACT

This paper describes an implementation of broadband soil attenuation in finite-difference time domain (FDTD) simulations of seismic wave propagation from impulsive sources. We concentrate on the attenuation phenomenon, the computational approach, comparisons with results from non-attenuating soil models, and the impacts on range estimation. Results are based on our three dimensional viscoelastic FDTD code *ptop*, which allows impulsive and moving vehicle simulations over realistic heterogeneous geologies and surface topographies.

Soil attenuation refers to the decay of seismic energy by intrinsic material losses in soil. It can reduce the amplitude of propagating waves and shift the frequency of signal energy, thus affecting vehicle range estimates and seismic signatures. Relative to other attenuation factors, i.e., geometric spreading and scattering, soil attenuation often dominates the total attenuation characteristics of seismic surface waves generated by moving vehicles.

*ptop* represents soil attenuation using the viscoelastic constitutive equations of a “standard linear solid” (SLS). The SLS form implemented is a material symbolized by a spring and dashpot in series that are in parallel with a spring. The viscous behavior of a standard linear solid can be characterized across a limited frequency band by the quality factors  $Q_p$  and  $Q_s$ , which are material properties that are inversely proportional to the attenuation coefficients of P- and S-waves, respectively.

For the frequency range of interest to seismic vehicle tracking, soils are known to have an approximately constant  $Q$ . To model broadband attenuation in our computations, each  $Q$  is defined in *ptop* by superimposing the band limited damping mechanisms of

## Report Documentation Page

<b>Report Date</b> 00 Sep 2001	<b>Report Type</b> N/A	<b>Dates Covered (from... to)</b> -
<b>Title and Subtitle</b> Soil Attenuation in Seismic Simulations: Implications for Vehicle Tracking		<b>Contract Number</b>
		<b>Grant Number</b>
		<b>Program Element Number</b>
<b>Author(s)</b>		<b>Project Number</b>
		<b>Task Number</b>
		<b>Work Unit Number</b>
<b>Performing Organization Name(s) and Address(es)</b> USACE Engineer Research and Development Center Cold Regions Research and Engineering Laboratory (ERDC-CRREL) 72 Lyme Rd Hanover, NH 03755		<b>Performing Organization Report Number</b>
		<b>Sponsor/Monitor's Acronym(s)</b>
<b>Sponsoring/Monitoring Agency Name(s) and Address(es)</b> Department of the Army, CECOM RDEC Night Vision & Electronic Sensors Directorate AMSEL-RD-NV-D 10221 Burbeck Road Ft. Belvoir, VA 22060-5806		<b>Sponsor/Monitor's Report Number(s)</b>
		<b>Distribution/Availability Statement</b> Approved for public release, distribution unlimited
<b>Supplementary Notes</b> See also ADM201471, Papers from the Meeting of the MSS Specialty Group on Battlefield Acoustic and Seismic Sensing, Magnetic and Electric Field Sensors (2001) Held in Applied Physics Lab, Johns Hopkins Univ, Laurel, MD on 24-26 Oct 2001. Volume 2 (Also includes 1999 and 2000 Meetings), The original document contains color images.		
<b>Abstract</b>		
<b>Subject Terms</b>		
<b>Report Classification</b> unclassified	<b>Classification of this page</b> unclassified	
<b>Classification of Abstract</b> unclassified	<b>Limitation of Abstract</b> UU	
<b>Number of Pages</b> 20		

$L$  standard linear solids at  $L$  selected frequencies so that the corresponding  $Q$  is approximately constant over a desired bandwidth. This results in a  $Q$  function that is consistent with observed attenuation in seismic surface waves.

We demonstrate *ptop*'s viscoelastic soil attenuation response through simulations of an impulsive source at the surface of a realistic geology and show how the source's spectral energy is shifted and absorbed. We further comment on the impact that soil attenuation has on target range estimates.

## 1. INTRODUCTION

The US Army is interested in the characteristics of seismic surface waves from moving armored vehicles. Systems such as Hornet, Raptor, and Rattler, and unattended ground sensor networks of the Future Combat System, will rely in part on measured seismic surface waves for successful operation. One feature of these waves is that they show smooth amplitude decay as a function of vehicle range (Moran and Greenfield, 1997, and Prado, 1998). As a consequence, tracking algorithms for estimating range-to-target using measured seismic signals are generating increasing interest (Moran et al., 1998).

In support of the Army's seismic sensing needs and its development of tracking algorithms, we are developing a high-fidelity numerical model for seismic wave propagation that considers the complex effects of topographical features, shallow geological structure, and material attenuation on propagating waves. Its results can be used, for example, in lieu of field data for developing, testing and refining tracking algorithms for networked seismic sensors (Moran et al., 2001).

Soil attenuation refers to the decay of seismic energy in propagating waves by intrinsic material losses in soil. It can reduce the amplitude of propagating waves and shift the frequency of signal energy, thus affecting vehicle range estimates and seismic signatures. Attenuation in near-surface soil is the focus of this paper. Specifically we describe soil attenuation as a phenomenon; our approach for including soil attenuation in our seismic wave propagation model and in the geologic models required as input; a demonstration of numerical seismic propagation with soil attenuation; and the impacts of soil attenuation on range estimation.

## 2. SOIL ATTENUATION

The propagation of small-strain seismic waves in soil is a small disturbance phenomenon that does not alter the fabric of the soil or cause permanent deformations (Santamarina et al., 2001). Nonetheless, energy of the small disturbances can be dissipated in heat, resulting in considerable changes in seismic waveforms. This dissipation is the loss phenomenon we call soil attenuation.

Soil attenuation is included in one of the three classes of attenuation mechanisms in seismic wave propagation: material, geometric, and apparent attenuation. Material attenuation refers to the dissipative loss phenomena of geologic materials, including soil. It occurs almost entirely in shear by small transverse movements of material lattices and grain boundaries (Lay and Wallace, 1995). Geometric attenuation is the spreading of wave energy as it propagates outward from a source. For surface waves, geometric spreading is cylindrical. Apparent attenuation includes scattering of energy by heterogeneous geologic and topographic features and partial energy

transmission across geologic interfaces (Santamarina et al., 2001). Apparent attenuation is the most difficult to quantify. Relative to the other classes, material attenuation—i.e., soil attenuation—often dominates the total attenuation characteristics of seismic surface waves generated by moving vehicles.

For a Rayleigh surface wave, the dependence of the particle velocity amplitude,  $A$ , on range,  $r$ , from the source, is of the form (Lay and Wallace, 1995)

$$A = [A_0] [r^{-1/2}] \left[ \exp\left(-\frac{\pi f r}{Qc}\right) \right] , \quad (1)$$

where  $A_0$  is a reference particle velocity amplitude;  $Q$  is a unitless “quality factor” that quantifies the material attenuation and, depending on the data, the apparent attenuation as well; and  $f$  and  $c$  are the frequency and wave speed of the propagating wave, respectively. As Equation 1 indicates, lower  $Q$  results in higher attenuation. Constant  $Q$ , over an applicable frequency bandwidth, is recognized to be the most physically realistic functional variation of  $Q$  to represent material attenuation in seismic wave propagation (e.g., Xu and McMechan, 1998).

Using Equation 1, Greenfield and Moran (2001) processed field-measured data sets over limited frequency bands to perform least-squares particle velocity amplitude versus range fits of the data. These fits—from five Army proving ground sites—are shown as amplitude in dB vs. range curves in Figure 1. The strong influence of geologic structure from site to site is evident. The figure shows large differences in both amplitude levels and in attenuation rate. The different amplitude levels are due principally to differences in material stiffness at the sites. The different attenuation rates, where there is overlap of the ranges of the data in the curves, can be due to differences in both material and scattering losses. Based upon the geology of the sites, however, differences in soil losses are likely to have had far greater influence in the slopes of the Figure 1 curves than differences in scattering losses. Thus, as the Figure 1 curves suggest, synthetic data to be used by researchers for developing range estimation algorithms should include the effects of soil attenuation on propagating waves.

### 3. COMPUTATIONAL APPROACH

Our work (e.g., Moran et al., 1999, Ketcham et al., 2000) modeling seismic wave propagation originated from the linear elastic formulations and numerical implementations described by Hestholm and Ruud (1998), who incorporated surface topography with an appropriate stress-free surface boundary condition into a finite-difference time domain (FDTD) wave propagation model featuring 8<sup>th</sup>-order, staggered-grid, finite-difference operators. To accommodate surface topography, Hestholm and Ruud express geologic models using a curvilinear grid that is transformed into a rectangular computational grid of equal grid spacing. This mapping can be visualized by proportionally stretching the rectangular grid in the vertical direction so that the free surface matches the topographic function. Appendix A provides a partial mathematical description of the Hestholm and Ruud (1998) elastic formulation. Specifically it describes the curved system, equations of motion, and stress-strain-velocity relationships.

To model soil absorption in finite difference seismic wave propagation calculations, geophysical researchers commonly use the theoretical framework of linear viscoelasticity. Relative to linear-elastic materials, linear-viscoelastic materials retain the linearity between stress and strain, but the relationship also includes time. A linear-elastic body has a simple memory—it “remembers” only its unstrained configuration, allowing the present deformation to be found knowing only the load.

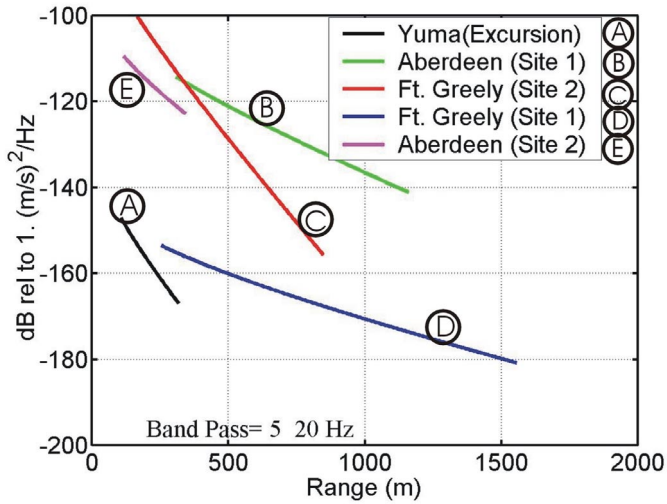


Figure 1. Vertical particle velocity amplitude vs. range fits of data from Army proving ground sites.

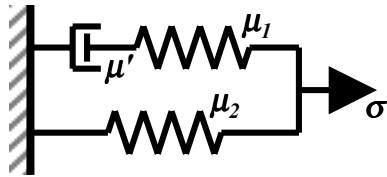


Figure 2. A “standard linear solid.”  $\mu'$  is viscosity,  $\mu_1$  and  $\mu_2$  are elastic moduli, and  $\sigma$  is stress.

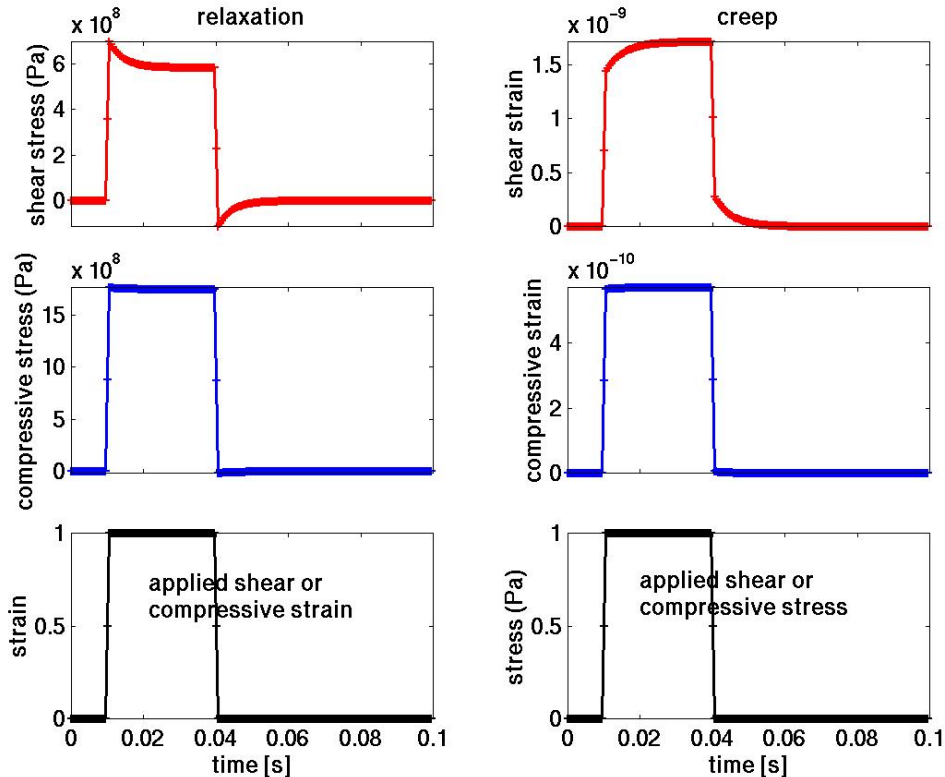


Figure 3. Relaxation and creep loading solutions to the stress-strain relation of the standard linear solid. The solid has material properties of the upper soil layer in the Figure 4 geologic model.

For a linear-viscoelastic body, however, the deformation cannot be determined unless the entire history of loading is known (Fung, 1965).

A linear-viscoelastic material is one for which infinitesimal strains, displacements, and velocities are considered and the stress tensor  $\sigma_{ij}(x,y,z,t)$  is related to the strain tensor  $\varepsilon_{kl}(x,y,z,t)$  by a convolution integral. This may be abbreviated in the equivalent forms

$$\sigma_{ij} = G_{ijkl} * d\varepsilon_{kl} / dt = \varepsilon_{kl} * dG_{ijkl} / dt , \quad (2)$$

where  $G_{ijkl}$  is the tensorial relaxation function of the material and  $*$  denotes convolution integral operations (Fung, 1965). For an isotropic material,  $G_{ijkl}$  can be defined by two scalar relaxation functions, one in isotropic compression,  $\Lambda$ , and one in shear,  $2 M$ , such that

$$\sigma_{ij} = d\Lambda / dt * \delta_{ij} \varepsilon_{kk} + 2 dM / dt * \varepsilon_{ij} . \quad (3)$$

Because the relaxation functions are scalar functions, it is appropriate to specify their behavior using analogies of common networks of springs and dashpots. Our FDTD seismic wave propagation code, *ptop*, implements viscoelasticity according to the finite difference formulations of Hestholm (1999) and Robertsson et al. (1994). These formulations use the constitutive equations of a “standard linear solid” (SLS) in the form symbolized by a “Maxwell element” (i.e., a spring and dashpot in series) that is in parallel with a spring. This is illustrated in Figure 2. In this figure  $\mu'$  is the viscosity of the solid, i.e., the proportionality constant between stress and the rate of strain, and  $\mu_1$  and  $\mu_2$  are elastic moduli of the solid, i.e., proportionality constants between stress and strain.  $\mu_2$  is the relaxed modulus corresponding to the long-time viscous response, while  $\mu_1 + \mu_2$  is the immediate, unrelaxed modulus. The stress-strain relation is (e.g., Fung, 1965)

$$\sigma + \tau_\varepsilon d\sigma / dt = \mu_2 ( \varepsilon + \tau_\sigma d\varepsilon / dt ) , \quad (4)$$

where  $\tau_\sigma$  and  $\tau_\varepsilon$  are the relaxation times for stress and strain, respectively, which are defined by

$$\tau_\sigma = \mu' (\mu_1 + \mu_2) / \mu_1 \mu_2 , \text{ and} \quad (5)$$

$$\tau_\varepsilon = \mu' / \mu_1 . \quad (6)$$

Solutions to the stress-strain relation are illustrated in Figure 3 for a Poisson solid, i.e., a material with Poisson ratio of 0.25. The solutions are for relaxation and creep loading. They have the forms

$$\sigma(t) = \mu_2 [ 1 - (1 - \tau_\varepsilon / \tau_\sigma) \exp(-t / \tau_\sigma) ] \mathbf{1}(t) , \quad (7)$$

for relaxation loading—i.e., a unit step application of strain, and

$$\sigma(t) = 1/\mu_2 [ 1 - (1 - \tau_\sigma / \tau_\varepsilon) \exp(-t / \tau_\varepsilon) ] \mathbf{1}(t) , \quad (8)$$

for creep loading—i.e., a unit step application of stress.  $\mathbf{1}(t)$  is the unit step function. Shear and compressive responses are depicted in Figure 3 for corresponding shear and compressive unit disturbances that are shown at the bottom of the figure. These disturbances are applied and removed as indicated. The responses shown are for a viscoelastic soil with shear wave speed = 577 m/s and density = 1750 kg/m<sup>3</sup>, one material considered in a geologic model to be described subsequently.

With reference to Equation 3, Robertsson et al. (1994) and Hestholm (1999) define  $\Pi = \Lambda + 2 M$ , and use the standard-linear-solid relaxation solutions

$$\Pi(t) = (\lambda + 2\mu) [ 1 - (1 - \tau_\varepsilon^p / \tau_\sigma) \exp(-t / \tau_\sigma) ] \mathbf{1}(t) , \text{ and} \quad (9)$$

$$M(t) = \mu [ 1 - (1 - \tau_\varepsilon^s / \tau_\sigma) \exp(-t / \tau_\sigma) ] \mathbf{1}(t) , \quad (10)$$

to define material behavior in their finite difference formulations. Here  $\lambda$  and  $\mu$  are Lame's elastic parameters,  $\tau_\varepsilon^P$  and  $\tau_\varepsilon^S$  are the strain relaxation times for P- and S-waves, respectively, and  $\tau_\sigma$  is the stress relaxation time for both P- and S-waves. Using these equations Robertsson et al. (1994) and Hestholm (1999) derived the viscoelastic stress-strain-velocity relations that are presented in Appendix B. These relations, relative to the elastic stress-strain-velocity relations in Appendix A, include the effects of relaxation times and memory variables on the stress. The memory variables,  $r_{ij}$ , relate the current value of stress to strain history, which is required for viscoelastic modeling. As indicated in Appendix B, Equations 9 and 10 can be generalized to represent the relaxation behavior of superpositioned SLS mechanisms.

From Figure 3 one can note that the relaxation of a Poisson standard linear solid is dominated by shear behavior, which is consistent with soil attenuation phenomena. Indeed, SLS spring and dashpot constants can be assigned so that soil absorption during seismic wave propagation can be realistically modeled. The SLS spring and dashpot configuration is commonly used because the viscous behavior can be characterized across a limited frequency band by the quality factors  $Q_p$  and  $Q_s$ , which are inversely proportional to the attenuation of P- and S-waves, respectively.

$Q_p$  and  $Q_s$  represent the attenuation of P- and S-waves in the following way; they refer to the fractional loss of energy per cycle of a P- or S-wave oscillation (Lay and Wallace, 1995), respectively. The inverse proportionality to the attenuation coefficients  $\alpha_p$  or  $\alpha_s$  is given by  $1/Q_p = \alpha_p \lambda_p / \pi$  for P-waves and  $1/Q_s = \alpha_s \lambda_s / \pi$  for S-waves, where  $\lambda_p$  and  $\lambda_s$  are the respective wavelengths.  $Q_p$  and  $Q_s$  can also be defined (Carcione et al., 1988, Xu and McMechan, 1998) in the frequency domain using the real and imaginary parts of the unrelaxed bulk and shear moduli. For the unrelaxed shear modulus,  $\mu_u$ , (which, at the instant of loading is analogous to  $\mu_1 + \mu_2$  for the SLS in Figure 2) this takes the  $1/Q$  form

$$Q_s^{-1}(f) = \text{Im}[\mu_u(f)] / \text{Re}[\mu_u(f)], \quad (11)$$

where  $f$  is frequency.  $\mu_u$ , for a single SLS mechanism, is defined as (Xu and McMechan, 1998)

$$\mu_u(f) = 2\mu \left[ (1 + i 2\pi f \tau_\varepsilon^s) / (1 + i 2\pi f \tau_\sigma^s) \right], \quad (12)$$

where  $\mu$  is the relaxed (elastic) shear modulus. Defining  $1/2\pi\tau_\sigma^s$  as the relaxation frequency  $f_R$ ,  $Q_s^{-1}$  for a single SLS mechanism is then (Xu and McMechan, 1998)

$$Q_s^{-1}(f) = - \frac{\left(1 - \frac{\tau_\varepsilon^s}{\tau_\sigma^s}\right) \frac{f/f_R}{1 + (f/f_R)^2}}{1 - \left(1 - \frac{\tau_\varepsilon^s}{\tau_\sigma^s}\right) \frac{(f/f_R)^2}{1 + (f/f_R)^2}}. \quad (13)$$

Xu and McMechan (1998) similarly define  $Q_p^{-1}$  and the unrelaxed bulk modulus. Their focus, however, is not on single SLS mechanisms but on the superposition of multiple SLS mechanisms in order to achieve nearly-constant  $Q$  to realistically represent material attenuation over the dominant frequency bandwidth of a given FDTD calculation. For  $L$  mechanisms, Equations 12 and 13 become (Xu and McMechan, 1998)

$$\mu_u(f) = 2\mu \left[ 1 - L + \sum_{l=1}^L \frac{1 + i 2\pi f \tau_{\varepsilon l}^s}{1 + i 2\pi f \tau_{\sigma l}^s} \right]. \quad (14)$$

$$Q_s^{-1}(f) = -\frac{\sum_{l=1}^L \left[ \left( 1 - \frac{\tau_{el}^s}{\tau_{ol}^s} \right) \frac{f / f_{RI}}{1 + (f / f_{RI})^2} \right]}{1 - \sum_{l=1}^L \left[ \left( 1 - \frac{\tau_{el}^s}{\tau_{ol}^s} \right) \frac{(f / f_{RI})^2}{1 + (f / f_{RI})^2} \right]} . \quad (15)$$

Again, Xu and McMechan (1998) similarly define  $Q_p^{-1}$  and the unrelaxed bulk modulus. They further describe an inversion technique to calculate appropriate relaxation times  $\tau_e^p$  and  $\tau_e^s$  for each mechanism. Their technique, automated in software (Ramos-Martinez et al., 2000), uses simulated annealing to find the combination of  $L$  relaxation mechanisms to best fit the desired  $Q$ . The relaxation frequencies are chosen according to the desired bandwidth where  $Q$  is to be nearly constant and are assigned identically for both P- and S-wave propagation.

Because the unrelaxed moduli are functions of frequency, the P- and S-wave speeds of the material vary with the frequency of oscillating disturbances. Typically, near surface geologic materials get stiffer with increasing frequency of loading. As one would expect from elastic material property definitions, P- and S-wave speeds increase with frequency as well. An expression for the unrelaxed shear wave speed,  $V_{su}$ , with frequency is (Carcione et al., 1988)

$$V_{su}(f) = \text{Re}[(\mu_u(f) / \rho)^{1/2}] . \quad (16)$$

A similar expression can be found for the unrelaxed compression wave speed.

Stress calculations using viscoelastic relations in Appendix B rather than the elastic relations in Appendix A are the principal difference between viscoelastic and elastic results from *ptop*. As commented in Appendix B, the calculations can be performed for  $L$  SLS mechanisms. For this case, an approach to define a material's viscoelastic properties can be outlined by:

- Select the desired constant  $Q_p$  and  $Q_s$  to define soil attenuation.
- Select relaxation frequencies  $f_R$  of  $L$  standard linear solid mechanisms to span the bandwidth where constant  $Q$  is desired.
- Find the P-wave and S-wave strain relaxation times  $\tau_e^p$  and  $\tau_e^s$  of each mechanism that provide near-constant values of  $Q$ , approximating constant  $Q_p$  and  $Q_s$ , over the selected bandwidth.

This is the approach used for the viscoelastic material definitions reported in this paper. We adopted the Xu and McMechan (1998) simulated annealing technique (Ramos-Martinez et al., 2000) to find the strain relaxation times of each mechanism.

## 4. DEMONSTRATION OF *PTOP*'S VISCOELASTIC SOIL ATTENUATION

Finite-difference seismic simulations over the expected range of coverage for FCS seismic unattended ground sensor systems require substantial models and computational durations. As a consequence, our simulations are parallel computations based upon a domain decomposition strategy (Moran et al., 1999). We perform computations on multi-processor computers available at DoD High Performance Computing Modernization Program centers. The simulations described in this paper were performed using a Cray T3E at the Army High Performance Computing Research Center. The geologic model, which is illustrated in Figure 4, has typical topographic and geologic features of the “hill and dale” class of research and development models we use for

testing the numerical robustness of *ptop*. Its size is roughly 350 m by 500 m by 80 m (deep). A 2.8-m node spacing defines the rectangular grid spacing in the W-E and S-N directions. A minimum of 1.6 m is the node spacing in the vertical direction, which is elongated to handle topography as defined in Appendix A. The side and bottom boundaries were set with a 21-cell-thick absorption layer (Cerjan et al., 1985), providing a reduction of at least –20 dB in reflecting wave particle energy. The simulations were tests of the long-duration stability of our viscoelastic code. The simulated durations were up to 12 s with time steps of 180  $\mu$ s.

#### 4.1 Geologic Model and Impulsive Source

The geologic model is a synthetic model consisting of two fairly stiff soil layers (above and below a water table) overlying granitic bedrock. It is similar to a model previously reported for demonstration of our moving impulsive source capability (Ketcham et al., 2000), yet larger in horizontal extent. Two common geological features distinguish its sloping topography: an outcropping of the bedrock and a trench representative of an eroded streambed. Figure 4a is a surface contour graph illustrating the topography and these features.

The outcrop is roughly elliptical with dimensions of 80 m by 200 m. Its peak is offset laterally from the center of the streambed by approximately 200 m. The streambed is roughly 100 m wide by 8 m deep. “Downhill” on the model is from North to South, i.e., from the top of Figure 1 to the bottom, as a 0.002 slope occurs over the model in this direction.

Figure 4b illustrates the subsurface layering of the model; it is a slice at the 185-m South-North coordinate. The shades of the model refer to different materials. The upper two layers away from the outcrop are the soil layers. The surface soil layer is approximately 11 m thick. The lower soil layer—i.e., the soil beneath the “water table”—is approximately 15 m thick. The actual values vary throughout the model, as the surface is not flat. In addition, both soil layers reduce in thickness adjacent to the outcrop due to the increasing elevation of the bedrock surface as it rises toward the outcrop, and the upper soil layer thins toward the streambed.

The outcrop features an upper weathered zone. This zone is depicted in Figure 4a by the shading changes beneath the outcrop. The uppermost nodes in this zone have seismic propagation properties identical to the surface soil layer. The properties vary linearly until the granitic layer properties are reached.

Table 1 lists the seismic properties of the three principal layers. The elastic properties P-wave speed, S-wave speed, and density are supplemented by the quality factors  $Q_p$  and  $Q_s$ .

**Table 1. Seismic properties of layer materials in geologic model.**

Layer	Compression-wave speed (m/s)	Shear-wave speed (m/s)	Density (kg/m <sup>3</sup> )	Material loss quality factors $Q_p, Q_s$
Upper soil	1000	577	1750	25, 9
Lower soil	1600	625	2000	30, 15
Granitic bedrock	3500	2333	2650	150, 67

Force input to the models was a near-surface vertical pulse with a maximum force of 1 N and a duration of approximately 0.03 s. It was located near the intersection of the W-E and N-S centers of the model, just west of the trench, at W-E=252 m, S-N=184.8 m, and elevation=70.3 m. The depth below the surface was 7.2 m.

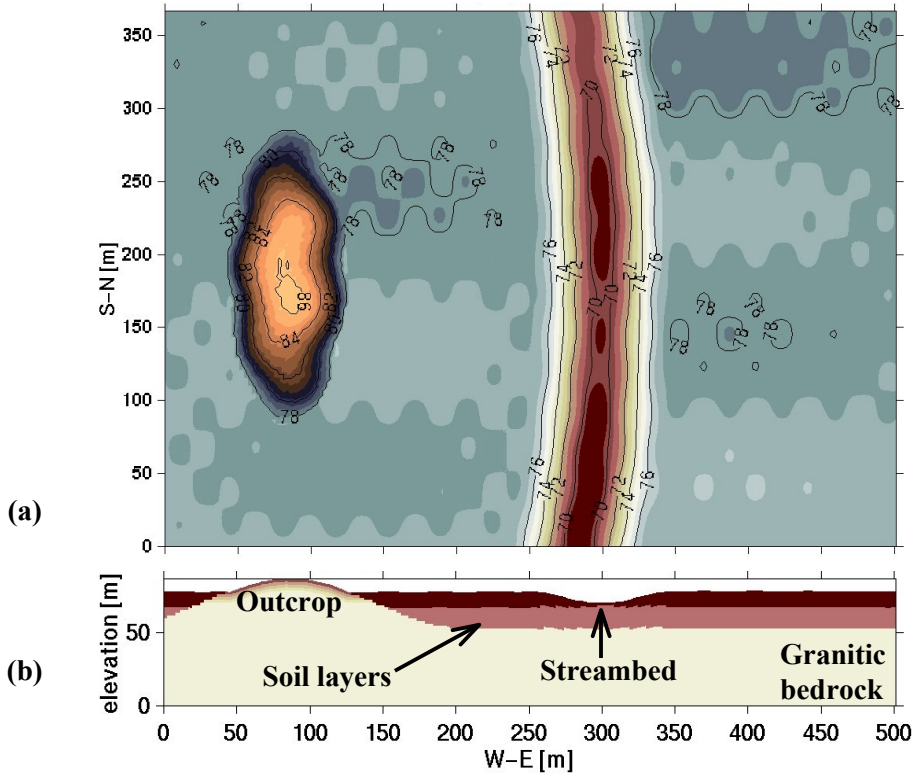


Figure 4. (a) Surface contour graph of geologic model with weathered bedrock outcrop, eroded streambed, and gently sloping flats. (b) Slice through model at South-North coordinate = 185 m.

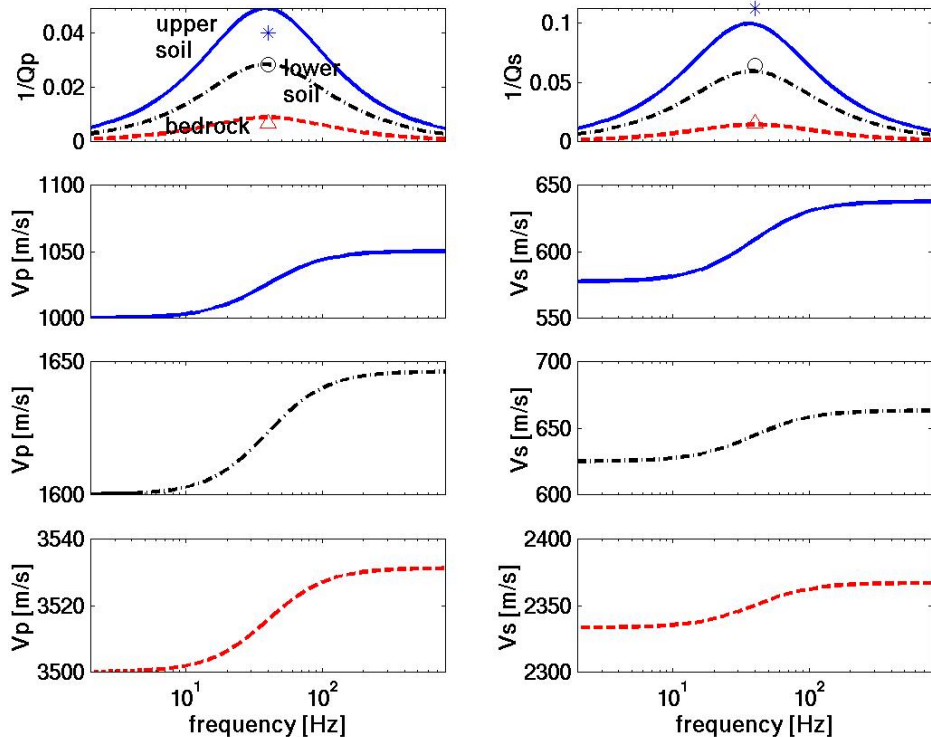


Figure 5. Spectra of  $Q_p^{-1}$ ,  $Q_s^{-1}$ , and unrelaxed P- and S-wave speeds for the 1-mechanism analysis tp1d\_fz1. Solid, dashdot, and dashed curves are respectively for the top-to-bottom layers in Table 1.

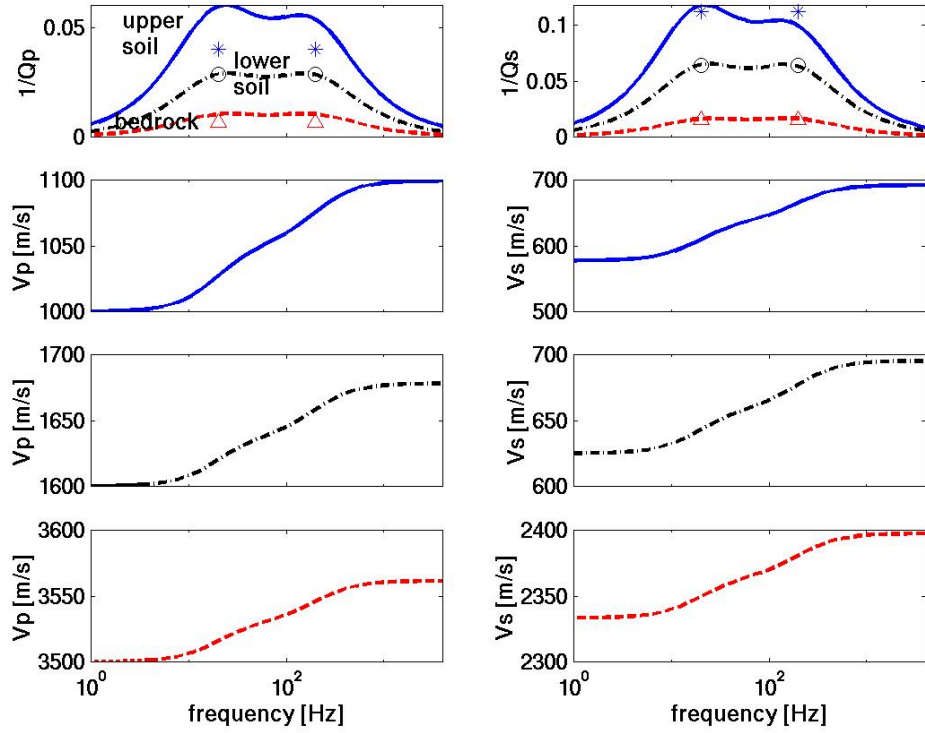


Figure 6. Spectra of  $Q_p^{-1}$ ,  $Q_s^{-1}$ , and unrelaxed P- and S-wave speeds for the 2-mechanism analysis tp1c\_fz1. Solid, dashdot, and dashed curves are respectively for the top-to-bottom layers in Table 1.

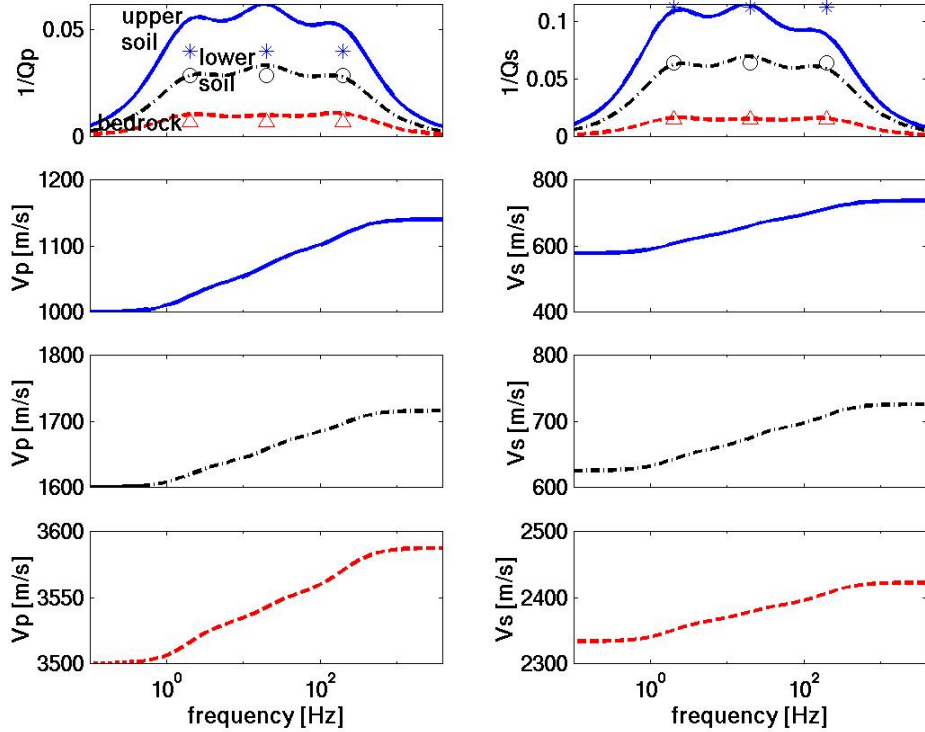


Figure 7. Spectra of  $Q_p^{-1}$ ,  $Q_s^{-1}$ , and unrelaxed P- and S-wave speeds for the 3-mechanism analysis tp1b\_fz1. Solid, dashdot, and dashed curves are respectively for the top-to-bottom layers in Table 1.

## 4.2 Simulations and Results

Three viscoelastic analyses and one elastic analysis are reported here for the geologic model and impulsive source described above. Table 2 presents the viscoelastic specifications that distinguish the analyses.

**Table 2. Elastic and viscoelastic simulations.**

Simulation ID	Analysis type	Number of SLS mechanisms	Relaxation frequencies (Hz)
tp1e_fz1	Elastic	0	N/A
tp1d_fz1	Viscoelastic	1	40
tp1c_fz1	Viscoelastic	2	20, 200
tp1b_fz1	Viscoelastic	3	2, 20, 200

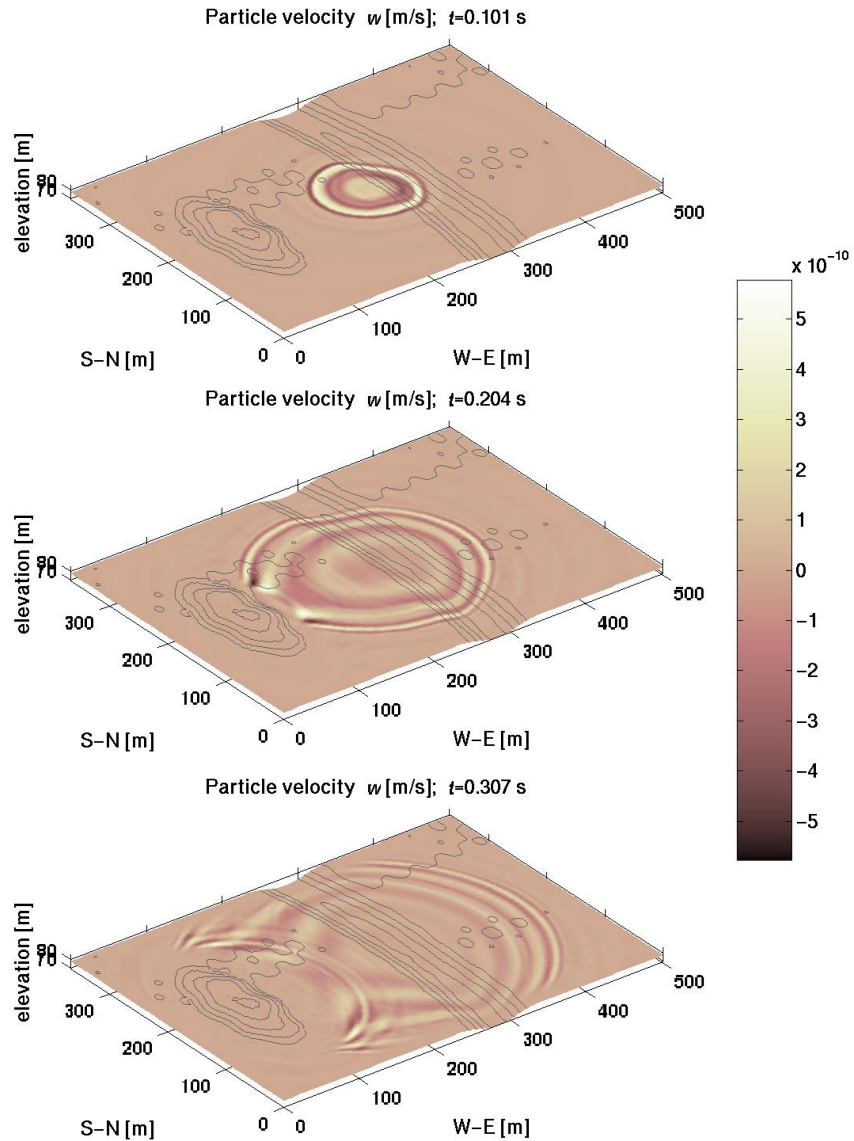
The three viscoelastic analyses, tp1d\_fz1, tp1c\_fz1 and tp1b\_fz1, use 1, 2 and 3 standard linear solid mechanisms, respectively, to represent the material attenuation behavior. The relaxation frequency of the 1-mechanism analysis corresponds to the center of dominant energy of the impulsive source. The frequencies of the 2- and 3-mechanism analyses span a widening bandwidth over which the model response was expected to be substantial.

Figure 5 illustrates spectra of  $Q_p^{-1}$  and  $Q_s^{-1}$  for the single-mechanism analysis. Curves are shown for the three main layers of the geologic model. These were calculated using the Xu and McMechan (1998) inversion technique (Ramos-Martinez et al., 2000). The peaks of the  $Q_p^{-1}$  and  $Q_s^{-1}$  curves in Figure 5 occur exactly at the 40-Hz relaxation frequency. Individual markers in the plots show the desired  $Q_p^{-1}$  and  $Q_s^{-1}$  values at the relaxation frequency. Comparisons of the markers with the spectra reveal that the inversion fits at their peak are accurate for the lower soil and bedrock, but have noticeable error for the upper soil with the highest  $1/Q$  values. Considering inaccuracies that occur in the estimation of  $Q$  from field data, the error is not excessive.

The lower three plots of each side in Figure 5 show, from top to bottom, the spectra of the unrelaxed P- and S-wave speeds of the upper soil layer, the lower soil layer, and the bedrock, respectively, that are predicted by Equation 16 and its P-wave counterpart. The increases in wave speeds with frequency are clear.

Figures 6 and 7 show spectral quantities corresponding to those plotted in Figure 5 for the 2- and 3-mechanism viscoelastic analyses. In these figures, however, the frequency bands are increasingly wider. As for the 1-mechanism analysis there is error observed in the  $Q^{-1}$  spectral peaks relative to the desired values, but the error is considerable mostly for  $Q_p^{-1}$  in the upper soil. The lower plots in these figures again show the increases in unrelaxed wave speeds of the three layers with frequency. Here the increases are sustained over the wider bandwidths, and are thereby greater.

Figure 8 depicts images of the vertical particle velocity,  $w$ , on the surface of the geologic model. The results are from the 2-mechanism viscoelastic analysis. These are shown at three times during the propagation of seismic waves from the impulsive source. A scale in the figure gives the correspondence between the image shade and the velocity amplitude in m/s. The center of the scale is 0 m/s. Lighter shades indicate positive/upward velocities and darker shades indicate negative/downward velocities. The principal waveforms displayed in the images are fundamental Rayleigh surface waves, which have cylindrical decay ( $1/r^{1/2}$ ,  $r$ =radius from source) in the absence of the topography and geology that disturb this decay. The waveforms reveal the geology-induced diffraction, refraction and reflection of the waves.



**Figure 8.** Images of vertical particle velocity  $w$  on geologic model surface at 0.1 s, 0.2 s, and 0.3 s. Image shade corresponds to value of  $w$  in scale. Contour lines are at 2-m intervals.

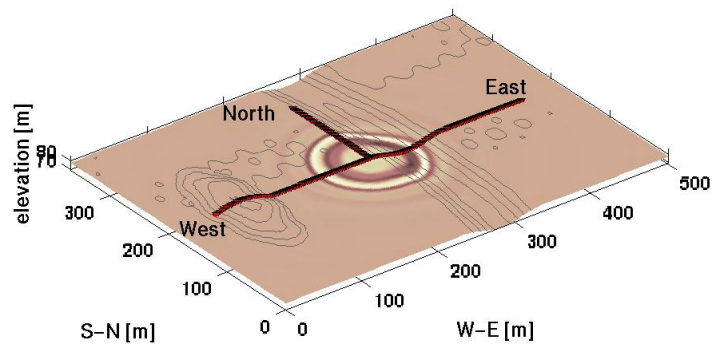


**Figure 9.** Location of three lines of “receivers” on the surface of the geologic model. The lines are labeled West, East, and North to indicate their direction from the source epicenter.

The Figure 8 images were constructed from the output of the 2-mechanism simulation at each finite-difference grid point on the surface, providing a spatial resolution of 2.8 m. Figure 9 shows another image, this from the elastic simulation, with three lines of “receivers” on the surface of the model. The lines are labeled West, East, and North to indicate their direction from the source epicenter. To compare the elastic and viscoelastic results,  $w$  versus time signals were collected from the full output of the analyses at the illustrated locations. As examples of the early  $w$  responses from the simulations, Figure 10 shows elastic and 2-mechanism viscoelastic signals from three of the locations: one at the epicenter (Figure 10a), one along the north line at 50-m range (Figure 10b), and another along the north line at 100-m range (Figure 10c).

The large early features of the Figure 10b and c waveforms are the Rayleigh surface waves. The attenuation relative to the elastic waveforms and the effect of the increasing wave speed with frequency shown in Figure 6 are evident. The Rayleigh wave speed for the upper soil layer of the elastic analysis is 530 m/s (Rayleigh wave speed  $V_R = 0.92 V_s$  for this Poisson solid). For a 100-m range this would arrive at 0.19 s, which is consistent with what the 100-m range signal in Figure 10a shows. The Rayleigh wave arrival for the 2-mechanism analysis is earlier, suggesting an unrelaxed surface wave speed of around 600 m/s and therefore a shear wave speed of 650 m/s. Indeed, the shear wave speed for the upper soil layer in Figure 6 is close to 650 m/s in the frequency bandwidth of interest. The later, oscillating features of the Figure 10b and c waveforms appear to be resonant vibrations associated with guided energy, i.e., energy that is mostly trapped in the soil layers.

Figure 11a and b present magnitudes of cross spectra between the epicenter signals of Figure 10a and the 50- and 100-m range signals in Figures 10b and 10c. The elastic results are shown on the left in the figure, and the 2-mechanism viscoelastic results are shown on the right. Shifts in the dominant spectral peaks toward higher frequencies from the cross spectra of the elastic signals to the viscoelastic signals are evident, as are reductions in spectral amplitude relative to the reference signal at 0-m range. It is clear that spectral response quantities are affected by modeled soil attenuation.

## 5. IMPACTS ON RANGE ESTIMATION

Figure 12 illustrates maximum signal amplitude (zero-to-peak vertical particle velocity  $w$ ) from the three geophone lines depicted in Figure 9. The results in each plot are from the four FDTD analyses detailed in Table 2. The figure highlights the impacts that attenuation mechanisms have on simulated amplitude versus range data. In each plot the elastic result has the highest vertical particle velocity amplitudes over the range shown. The curves reduce noticeably in amplitude as 1-, 2-, and 3-mechanisms are added, although the reduction appears greatest when adding one and then two mechanisms. This result substantiates the previous statement made upon examination of the Figure 1 field data curves, i.e., that synthetic data to be used by researchers for developing range estimation algorithms should include the effects of soil attenuation on propagating waves.

Figure 12 also reveals the considerable impact that geologic and topographic features can have on particle velocity amplitude versus range data. The West line shows a sudden drop in amplitude as the soil thickness becomes small near the bedrock outcrop. Figure 4 shows the section of the subsurface geology beneath this line. It is at a range of just over 100 m where the amplitude drops steeply, which is just what one would expect by looking at the Figure 4 section. The East line shows no dramatic change as the trench is encountered, but relative to the West and North lines, it is evident that the trench has the effect of reducing vertical particle velocity amplitudes at ranges of approximately 100 m and less.

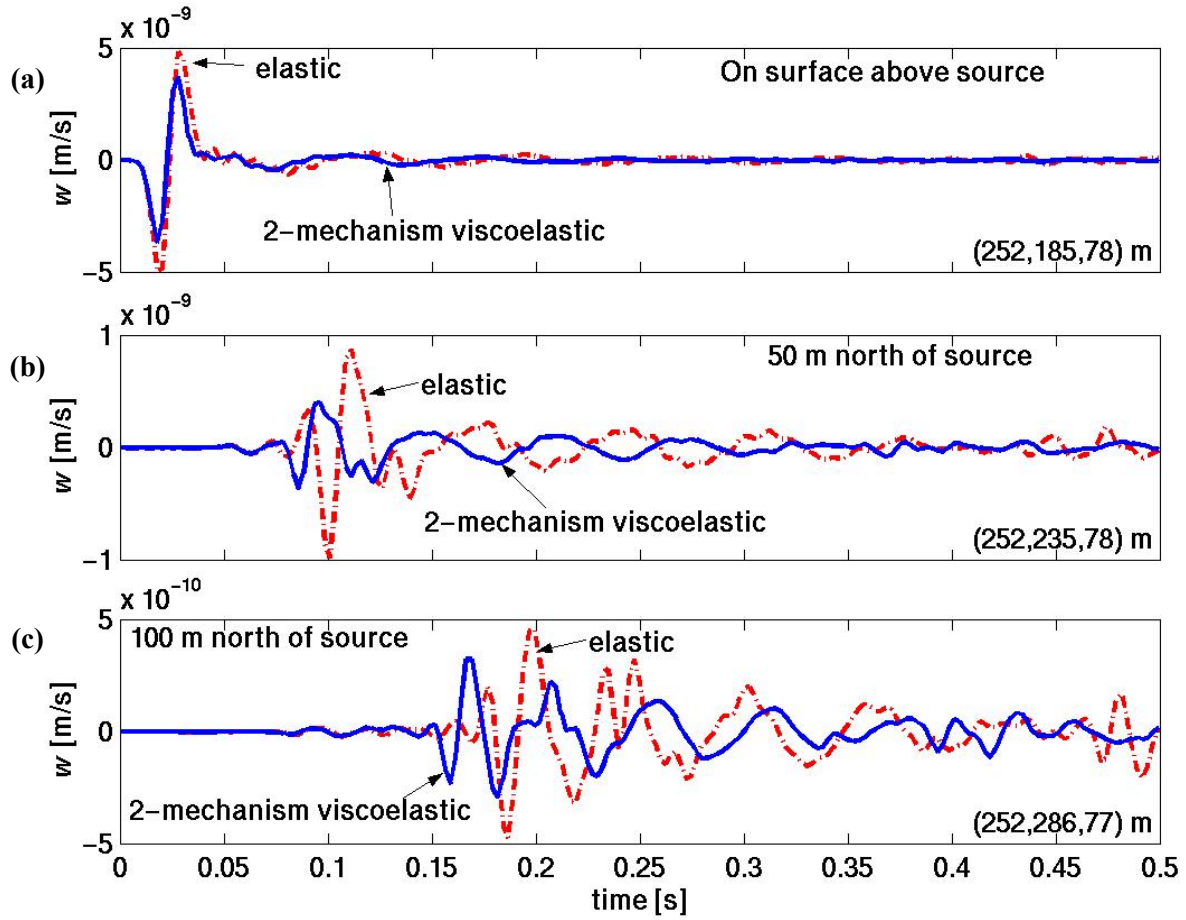


Figure 10. Elastic and 2-mechanism viscoelastic signals from three “North line” receiver locations:  
 (a) the epicenter, (b) 50-m range, and (c) 100-m range .

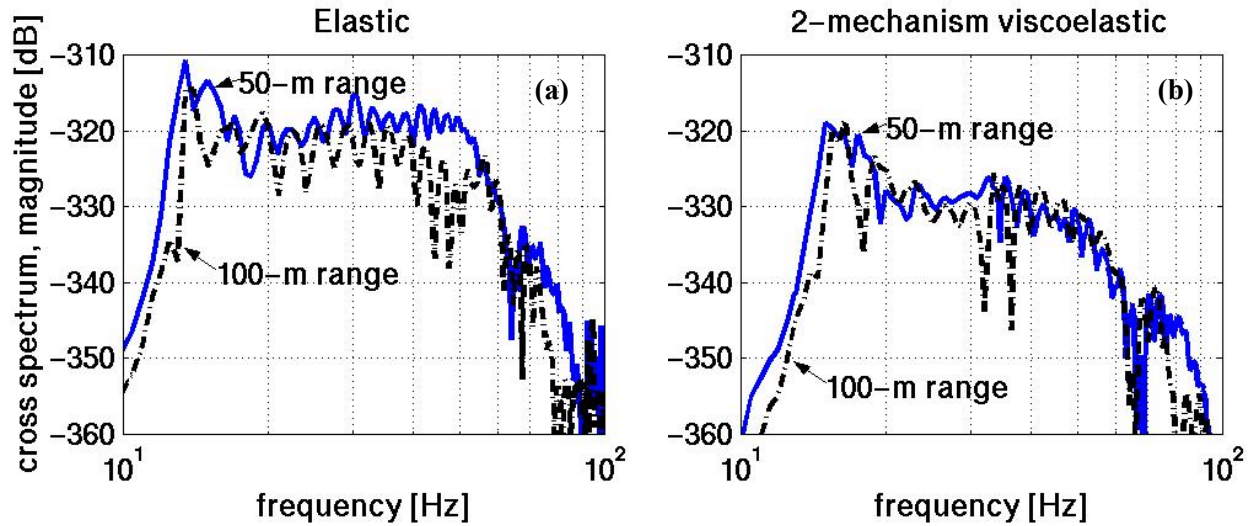
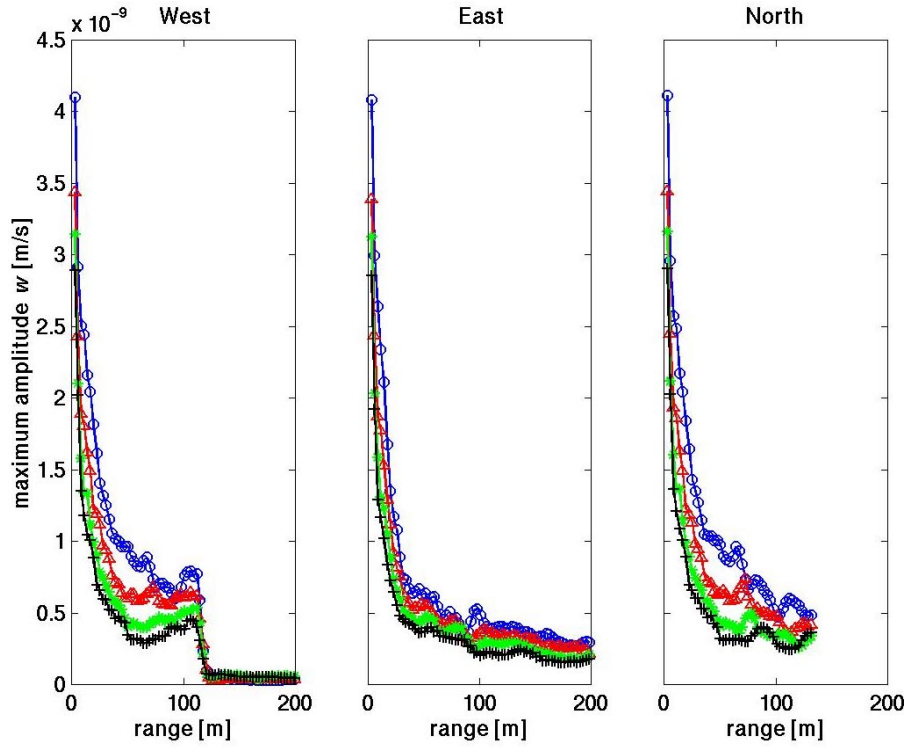
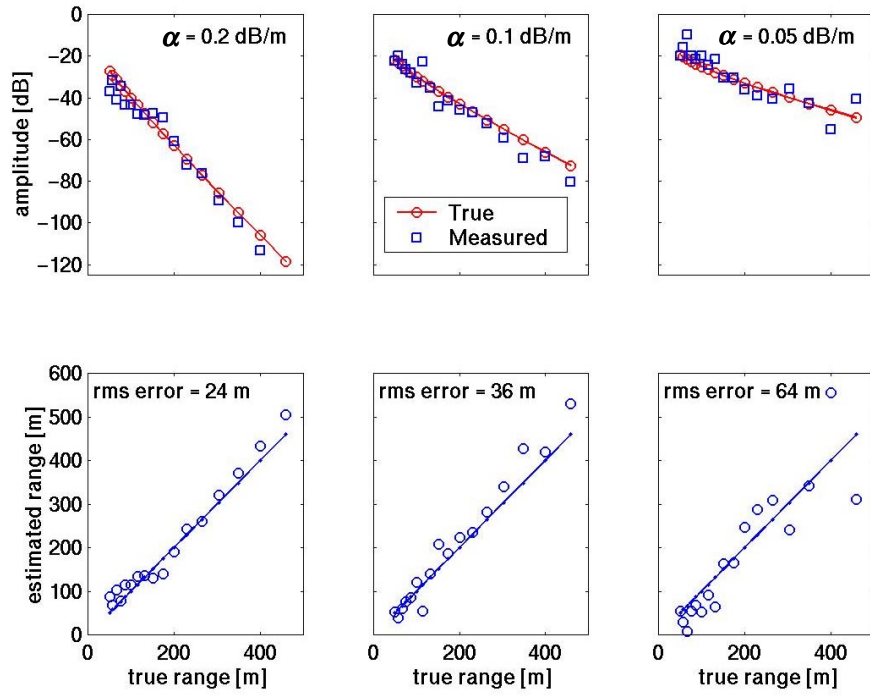


Figure 11. Cross spectra magnitudes between the epicenter signals of Figure 10a and the 50- and 100-m range signals in Figures 10b and 10c. (a) Elastic and (b) 2-mechanism viscoelastic results.



**Figure 12. Maximum signal amplitudes from the West, East, and North receiver lines. Results from the elastic analysis are the top lines with circle symbols. The 1-, 2-, and 3-mechanism viscoelastic results plot from top (triangle symbol) to bottom (plus symbol) below the elastic result, respectively.**



**Figure 13. Sets of true and measured amplitude versus range curves (top plots) and estimated range versus true range curves (bottom plots) for three hypothetical field sites with soil attenuation rates 0.2 dB/m (left plots), 0.1 dB/m (middle plots), and 0.05 dB/m (right plots).**

Figure 12 makes clear that attenuation due to both soil losses and scattering are important to model when producing synthetic results for developing ground sensor range estimation algorithms. Another issue—with direct field implications—is how different attenuation rates at different sites can affect estimates of range. For example, consider two sites that have identical particle velocity amplitude measurements in dB at some arbitrary range, but that have soils with significantly different attenuation rates. For the case where site “one” has a higher attenuation rate than site “two,” the errors in range estimation will be lower at site one due simply to the steeper slope of the attenuation curve at site one. In Figure 13 we present results of an exercise with three sites to illustrate this.

Figure 13 shows sets of curves for three hypothetical field settings that are distinguished solely by the soil attenuation rate  $\alpha$ . The three rates are 0.2, 0.1, and 0.05 dB/m, which represent a realistic range of attenuation rates that can be observed in field tests in different geologies.

An applicable form for particle velocity amplitude  $A$  versus range  $r$ , derivable from Equation 1, is  $A = A_0 r^{1/2} \exp(-\alpha r)$ , where  $\alpha$  is the attenuation rate in dB/m and  $A_0$  is a reference amplitude. For the three settings we define the error in estimating the signal amplitude to have a standard deviation of 5 dB. Perfect amplitude versus range data are generated, which are depicted by the “true” data in the upper plots of Figure 13, and normally distributed random error at the 5 dB level is added. The data with error are used to estimate the range as if they were measured data, and they are so designated in Figure 13a, c, and e. The estimated ranges, based upon a range estimation algorithm, are shown in the bottom plots of Figure 13 relative to the true ranges. rms errors in the range estimates are listed in the bottom plots. These data are repeated in Table 3.

The rms errors decrease with increasing attenuation rate. This is expected because as the attenuation rate increases, a constant error in the measured amplitude in dB leads to a smaller change in the estimated range.

**Table 3. Range estimation errors for different attenuation rates.**

$\alpha$ [dB/m]	rms error in range estimate [m]
0.05	64.2
0.1	35.8
0.2	24.3

The effect of soil attenuation on range estimation becomes more complicated in the presence of background seismic noise and complex geology. Nonetheless, where signals are above detectable levels, range estimates are likely to be more accurate in higher soil attenuation areas.

## 6. CONCLUSION

The viscoelastic seismic simulations we have presented demonstrate the effect of soil attenuation on seismic waveforms. The spectral energy from an impulsive source was increasingly absorbed and shifted as the number of relaxation mechanisms and bandwidth of the attenuation was increased. Because soil attenuation affects quantities of interest for range estimation and signature-spectra calculations, it is clear that synthetic data to be used by researchers for developing range estimation and signature identification algorithms should include the effects of soil attenuation on propagating waves.

The approach used for defining the broadband soil attenuation, i.e., the Xu and McMechan (1998) simulated annealing technique, proved an effective method for calculating relaxation times associated with desired quality factors and thereby defining the viscoelastic properties of our

geologic models. Used in the context of our viscoelastic seismic wave propagation code *ptop*, we observed expected effects of  $Q_p$ ,  $Q_s$ , and unrelaxed P- and S-wave speeds on surface waveforms and spectra.

Finally, in a range estimating exercise using hypothetical amplitude versus range data with different attenuation rates, we addressed the impact of soil attenuation on range-to-target estimates. We observed that range estimates are likely to be more accurate in higher soil attenuation areas where signals are above detectable levels.

## 7. REFERENCES

Carcione, J., Kosloff, D., and Kosloff, R., 1988, Wave Propagation Simulation in a Linear Viscoelastic Medium, *Geophysics Journal*, V. 95, pp. 597-611.

Cerjan, C., Kosloff, R., and Reshef, M., 1985, A Nonreflecting Boundary Condition for Discrete Acoustic-Wave and Elastic-Wave Equations, *Geophysics*, V. 50, pp. 705-708.

Fung, Y., 1965, *Foundations of Solid Mechanics*, Prentice-Hall, Englewood Cliffs, NJ.

Greenfield, R., and Moran, M., 2001, Monte Carlo Simulation of Seismic Location Errors for Moving Vehicles, Preprint F-1 for 2001 Meeting of the MSS Specialty Group on Battlefield Acoustic and Seismic Sensing, Magnetic and Electric Field Sensors.

Hestholm, S., and Ruud, B., 1998, 3-D Finite-Difference Elastic Wave Modeling Including Surface Topography, *Geophysics*, V. 63, pp. 613-622.

Hestholm, S., 1999, Three-Dimensional Finite-Difference Viscoelastic Wave Modeling Including Surface Topography, *Geophysics Journal International*, V. 139, pp. 852-878.

Ketcham, S., Moran, M., and Greenfield, R., 2000, FDTD Seismic Simulation of Moving Tracked Vehicle, Proceedings of the 2000 Meeting of the MSS Specialty Group on Battlefield Acoustic and Seismic Sensing, Report 440000-195-X(1), ERIM International, Inc., Ann Arbor, MI, pp. 289-306.

Lay, T., and Wallace, T., 1995, *Modern Global Seismology*, Academic Press, San Deigo, CA.

Moran, M., and Greenfield, R., 1997, Seismic Detection of Military Operations, 97-CEP-511-1, U.S. Army Maneuver Support Battle Laboratory, Ft. Leonard Wood, MO.

Moran, M., Boulanger, P., Greenfield, R., Gilligan, T., 1998, Range Estimation with Seismic Sensors for Early Detection, Final report 98-CEP-0505, Maneuver Support Battle Lab, U.S. Army Engineer School, Ft. Leonard Wood, MO.

Moran, M., Ketcham, S., and Greenfield, R., 1999, Three Dimensional Finite-Difference Seismic Signal Propagation, Proceedings of the 1999 Meeting of the MSS Specialty Group on Battlefield Acoustic and Seismic Sensing, Report 440000-147-X, ERIM International, Inc., Ann Arbor, MI, pp. 1-12.

Moran, M., Greenfield, R., and Ketcham, S., 2001, Geologic Adaptation for Seismic Network Tracking, Preprint G-5 for 2001 Meeting of the MSS Specialty Group on Battlefield Acoustic and Seismic Sensing, Magnetic and Electric Field Sensors.

Prado, G., 1998, Presentation Materials and Personal Communications, Boston, MA, SenTech, Inc.

Ramos-Martinez, J., Xu, T., and McMechan, G., 2000, *velqpqs.f*, © University of Texas at Dallas.

Robertsson, J., Blanch, J., and Symes, W., 1994, Viscoelastic Finite-Difference Modeling, *Geophysics*, V. 59, pp. 1444–1456.

Santamarina, J., Klein, K., and Fam, M., 2001, *Soils and Waves*, Wiley, Chichester, England.

Xu, T., and McMechan, G., 1998, Efficient 3-D Modeling with Application to Near-Surface Land Seismic Data, *Geophysics*, V. 63, pp. 601-612.

## 8. ACKNOWLEDGMENTS

This work was supported by the US Army Office of the Program Manager for Mines, Countermines, and Demolitions in support of Hornet, Raptor, and Rattler-Track3 under MIPR1FPIC00544 and MIPR1APIC0051. Additional funding was given by the US Army Corps of Engineers, Engineering Research and Development Center, Cold Regions Research and Engineering Laboratory (ERDC-CRREL) under PE62784/AT42. Work at Pennsylvania State University was supported by contract DACA89-99-C-0001 with ERDC-CRREL. Computational resources were provided by the Department of Defense High Performance Computing Modernization Program.

## APPENDIX A. ELASTIC FDTD FORMULATION (HESTHOLM AND RUUD, 1998)

Curved system  $x, y, z$  with topography function  $z_0(x, y)$ , and rectangular system  $\xi, \kappa, \eta$  :

$$\xi = x, \quad \kappa = y, \quad \eta = \eta_{\max} \frac{z}{z_0(x, y)}; \quad x = \xi, \quad y = \kappa, \quad z = \frac{\eta}{\eta_{\max}} z_0(x, y);$$

Partial derivatives needed in transformed medium equations :

$$\begin{aligned} \frac{\partial \eta}{\partial x} &= -\frac{\eta}{z_0(\xi, \kappa)} \frac{\partial z_0(\xi, \kappa)}{\partial \xi} \equiv A(\xi, \kappa, \eta), \quad \frac{\partial \eta}{\partial y} = -\frac{\eta}{z_0(\xi, \kappa)} \frac{\partial z_0(\xi, \kappa)}{\partial \kappa} \equiv B(\xi, \kappa, \eta), \\ \frac{\partial \eta}{\partial z} &= \frac{\eta_{\max}}{z_0(\xi, \kappa)} \equiv C(\xi, \kappa). \end{aligned}$$

Equations of motion in  $(\xi, \kappa, \eta)$  space :

$$\begin{aligned} \rho \frac{\partial u}{\partial t} &= \frac{\partial \sigma_{xx}}{\partial \xi} + A(\xi, \kappa, \eta) \frac{\partial \sigma_{xx}}{\partial \eta} + \frac{\partial \sigma_{xy}}{\partial \kappa} + B(\xi, \kappa, \eta) \frac{\partial \sigma_{xy}}{\partial \eta} + C(\xi, \kappa) \frac{\partial \sigma_{xz}}{\partial \eta} + f_x, \\ \rho \frac{\partial v}{\partial t} &= \frac{\partial \sigma_{xy}}{\partial \xi} + A(\xi, \kappa, \eta) \frac{\partial \sigma_{xy}}{\partial \eta} + \frac{\partial \sigma_{yy}}{\partial \kappa} + B(\xi, \kappa, \eta) \frac{\partial \sigma_{yy}}{\partial \eta} + C(\xi, \kappa) \frac{\partial \sigma_{yz}}{\partial \eta} + f_y, \\ \rho \frac{\partial w}{\partial t} &= \frac{\partial \sigma_{xz}}{\partial \xi} + A(\xi, \kappa, \eta) \frac{\partial \sigma_{xz}}{\partial \eta} + \frac{\partial \sigma_{yz}}{\partial \kappa} + B(\xi, \kappa, \eta) \frac{\partial \sigma_{yz}}{\partial \eta} + C(\xi, \kappa) \frac{\partial \sigma_{zz}}{\partial \eta} + f_z. \end{aligned}$$

Elastic stress - strain - velocity relationships in  $(\xi, \kappa, \eta)$  space :

$$\begin{aligned} \frac{\partial \sigma_{xx}}{\partial t} &= (\lambda + 2\mu) \left( \frac{\partial u}{\partial \xi} + A(\xi, \kappa, \eta) \frac{\partial u}{\partial \eta} \right) + \lambda \left( \frac{\partial v}{\partial \kappa} + B(\xi, \kappa, \eta) \frac{\partial v}{\partial \eta} + C(\xi, \kappa) \frac{\partial w}{\partial \eta} \right), \\ \frac{\partial \sigma_{yy}}{\partial t} &= \lambda \left( \frac{\partial u}{\partial \xi} + A(\xi, \kappa, \eta) \frac{\partial u}{\partial \eta} + C(\xi, \kappa) \frac{\partial w}{\partial \eta} \right) + (\lambda + 2\mu) \left( \frac{\partial v}{\partial \kappa} + B(\xi, \kappa, \eta) \frac{\partial v}{\partial \eta} \right), \\ \frac{\partial \sigma_{zz}}{\partial t} &= \lambda \left( \frac{\partial u}{\partial \xi} + A(\xi, \kappa, \eta) \frac{\partial u}{\partial \eta} + \frac{\partial v}{\partial \kappa} + B(\xi, \kappa, \eta) \frac{\partial v}{\partial \eta} \right) + (\lambda + 2\mu) C(\xi, \kappa) \frac{\partial w}{\partial \eta}, \\ \frac{\partial \sigma_{xy}}{\partial t} &= \mu \left( \frac{\partial v}{\partial \xi} + A(\xi, \kappa, \eta) \frac{\partial v}{\partial \eta} + \frac{\partial u}{\partial \kappa} + B(\xi, \kappa, \eta) \frac{\partial u}{\partial \eta} \right), \\ \frac{\partial \sigma_{xz}}{\partial t} &= \mu \left( \frac{\partial w}{\partial \xi} + A(\xi, \kappa, \eta) \frac{\partial w}{\partial \eta} + C(\xi, \kappa) \frac{\partial u}{\partial \eta} \right), \\ \frac{\partial \sigma_{yz}}{\partial t} &= \mu \left( \frac{\partial w}{\partial \kappa} + B(\xi, \kappa, \eta) \frac{\partial w}{\partial \eta} + C(\xi, \kappa) \frac{\partial v}{\partial \eta} \right) \end{aligned}$$

where :  $\rho$  is density,  $\lambda = \rho(V_p^2 - 2V_s^2)$  and  $\mu = \rho V_s^2$  are Lame's parameters for isotropic material with compression wave speed  $V_p$  and shear wave speed  $V_s$ ;  $f_x, f_y$ , and  $f_z$  are the components of the body force;  $u, v$ , and  $w$  are the components of the particle velocity; and  $\sigma_{xx}, \sigma_{yy}, \sigma_{zz}, \sigma_{xy}, \sigma_{xz}$ , and  $\sigma_{yz}$  are the stress components.

## APPENDIX B. VISCOELASTIC STRESS-STRAIN-VELOCITY RELATIONSHIPS (HESTHOLM, 1999)

$$\begin{aligned}
 \frac{\partial \sigma_{xx}}{\partial t} &= \Pi \frac{\tau_\varepsilon^P}{\tau_\sigma} \left( \frac{\partial u}{\partial \xi} + A(\xi, \kappa, \eta) \frac{\partial u}{\partial \eta} + \frac{\partial v}{\partial \kappa} + B(\xi, \kappa, \eta) \frac{\partial v}{\partial \eta} + C(\xi, \kappa) \frac{\partial w}{\partial \eta} \right) \\
 &\quad - 2M \frac{\tau_\varepsilon^S}{\tau_\sigma} \left( \frac{\partial v}{\partial \kappa} + B(\xi, \kappa, \eta) \frac{\partial v}{\partial \eta} + C(\xi, \kappa) \frac{\partial w}{\partial \eta} \right) + r_{xx}, \\
 \frac{\partial \sigma_{yy}}{\partial t} &= \Pi \frac{\tau_\varepsilon^P}{\tau_\sigma} \left( \frac{\partial u}{\partial \xi} + A(\xi, \kappa, \eta) \frac{\partial u}{\partial \eta} + \frac{\partial v}{\partial \kappa} + B(\xi, \kappa, \eta) \frac{\partial v}{\partial \eta} + C(\xi, \kappa) \frac{\partial w}{\partial \eta} \right) \\
 &\quad - 2M \frac{\tau_\varepsilon^S}{\tau_\sigma} \left( \frac{\partial u}{\partial \xi} + A(\xi, \kappa, \eta) \frac{\partial u}{\partial \eta} + C(\xi, \kappa) \frac{\partial w}{\partial \eta} \right) + r_{yy}, \\
 \frac{\partial \sigma_{zz}}{\partial t} &= \Pi \frac{\tau_\varepsilon^P}{\tau_\sigma} \left( \frac{\partial u}{\partial \xi} + A(\xi, \kappa, \eta) \frac{\partial u}{\partial \eta} + \frac{\partial v}{\partial \kappa} + B(\xi, \kappa, \eta) \frac{\partial v}{\partial \eta} + C(\xi, \kappa) \frac{\partial w}{\partial \eta} \right) \\
 &\quad - 2M \frac{\tau_\varepsilon^S}{\tau_\sigma} \left( \frac{\partial u}{\partial \xi} + A(\xi, \kappa, \eta) \frac{\partial u}{\partial \eta} + \frac{\partial v}{\partial \kappa} + B(\xi, \kappa, \eta) \frac{\partial v}{\partial \eta} \right) + r_{zz}, \\
 \frac{\partial \sigma_{xy}}{\partial t} &= M \frac{\tau_\varepsilon^S}{\tau_\sigma} \left( \frac{\partial v}{\partial \xi} + A(\xi, \kappa, \eta) \frac{\partial v}{\partial \eta} + \frac{\partial u}{\partial \kappa} + B(\xi, \kappa, \eta) \frac{\partial u}{\partial \eta} \right) + r_{xy}, \\
 \frac{\partial \sigma_{xz}}{\partial t} &= M \frac{\tau_\varepsilon^S}{\tau_\sigma} \left( \frac{\partial w}{\partial \xi} + A(\xi, \kappa, \eta) \frac{\partial w}{\partial \eta} + C(\xi, \kappa) \frac{\partial u}{\partial \eta} \right) + r_{xz}, \\
 \frac{\partial \sigma_{yz}}{\partial t} &= M \frac{\tau_\varepsilon^S}{\tau_\sigma} \left( \frac{\partial w}{\partial \kappa} + B(\xi, \kappa, \eta) \frac{\partial w}{\partial \eta} + C(\xi, \kappa) \frac{\partial v}{\partial \eta} \right) + r_{yz},
 \end{aligned}$$

where  $\Pi$  is the relaxation modulus for P - waves corresponding to  $\lambda + 2\mu$  in the elastic case and  $M$  is the relaxation modulus for S - waves corresponding to  $\mu$  in the elastic case;  $\tau_\varepsilon^P$  and  $\tau_\varepsilon^S$  are the strain relaxation times for P - and S - waves, respectively;  $\tau_\sigma$  is the stress relaxation time for both P - and S - waves; and  $r_{xx}$ ,  $r_{yy}$ ,  $r_{zz}$ ,  $r_{xy}$ ,  $r_{xz}$  and  $r_{yz}$  are memory variables relating current value of stress to strain history. For superposition of  $L$  mechanisms, summations are performed in the equations above, with the relaxation moduli defined by

$$\Pi = (\lambda + 2\mu) \left( 1 - \sum_{l=1}^L \left( 1 - \frac{\tau_{el}^P}{\tau_\sigma} \right) e^{-t/\tau_{el}} \right) l(t),$$

$$M = \mu \left( 1 - \sum_{l=1}^L \left( 1 - \frac{\tau_{el}^S}{\tau_\sigma} \right) e^{-t/\tau_{el}} \right) l(t),$$

where  $l(t)$  is the Heaviside or unit step function.